2019-24-0095 Published 09 Sep 2019

CFD Modeling of Gas Exchange, Fuel-Air Mixing and Combustion in Gasoline Direct-Injection Engines

Tommaso Lucchini, Gianluca D'Errico, Davide Paredi, Lorenzo Sforza, and Angelo Onorati
Politecnico di Milano

Citation: Lucchini, T., D'Errico, G., Paredi, D., Sforza, L. et al., "CFD Modeling of Gas Exchange, Fuel-Air Mixing and Combustion in Gasoline Direct-Injection Engines," SAE Technical Paper 2019-24-0095, 2019, doi:10.4271/2019-24-0095.

Abstract

Gasoline, direct injection engines represent one of the most widely adopted powertrain for passenger cars. However, further development efforts are necessary to meet the future fuel consumption and emission standards imposing an efficiency increase and a reduction of particulate matter emissions. Within this context, computational fluid dynamics is nowadays a consolidated tool to support engine design; this work is focused on the development of a set of CFD models for the prediction of combustion in modern GDI engines. The one-equation Weller model coupled with a zero-dimensional approach to handle initial flame kernel growth was applied to predict flame propagation. To account for mixture fraction fluctuations which might lead to the presence of soot precursor species, burned gas chemical composition is computed using tabulated kinetics with a presumed probability density function. Assessment of the combustion model was done with experimental data of flame radius evolution at different operating conditions. Afterwards, simulations were carried out for a turbocharged gasoline, direct-injection engine with a variable valve actuation. Different operating points were considered including variations of speed and load: a detailed comparison was performed between computed and experimental data of in-cylinder pressure and apparent heat release rate.

Introduction

For many years to come, spark-ignition engines will continue to be the main propulsion system for passenger cars thanks to their high power-to-weight ratio, fuel flexibility, simplified aftertreatment systems and easy integration with different levels of electrification to achieve a further fuel consumption reduction at relatively low costs [1]. However, further development work is needed to match the future CO_2 reduction targets by improving the engine thermal efficiency in all engine map, keeping low levels of pollutant emissions [2, 3]. To achieve such objectives, it is necessary to further optimize the combustion process, by taking different actions including compression ratio increase, geometry optimization, better knock control, optimized injection strategies, lean combustion operation, advanced ignition systems and, eventually, water injection [4, 5, 6, 7, 8].

Due to the very large number of involved parameters, the use of multi-dimensional numerical models is mandatory for a correct definition of a suitable engine layout in a reasonable amount of time. The complete engine cycle must be simulated, including also the combustion process, since engine efficiency and pollutant emissions are relevant results of the design process. However, simulation of the full-cycle in GDI engines is a very complex task for CFD modeling. The evolution of a reactive, multiphase and turbulent flow should be described inside a complex geometry and all these aspects impose severe stability and accuracy requirements. New modeling challenges arise from recent engine developments. Robust mesh management techniques are necessary to model the gas exchange process in VVA engines which can be characterized by very small valve lift or steep valve closure ramps [9]. Accurate boundary conditions, eventually together with the simulation of multiple cycles, are necessary for a correct estimation of the trapped in-cylinder air-fuel ratio under Miller cycle operation or when combined port-fuel and direct-injection strategies are adopted [10]. Regardless of the employed combustion model, the quality of the results strictly depends on the predicted in-cylinder charge motions, fuel distribution and turbulence intensity. Different approaches are available to predict flame propagation in spark-ignition engines, with the main challenges being represented by the description of the initial combustion stage and identification of a suitable expression for the turbulent flame speed [11, 12, 13, 14, 15]. In the event that the main pollutant emissions are to be assessed, the composition of the burned gas must be calculated in detail including the main soot precursors.

This paper is focused on CFD modeling of combustion in gasoline, direct-injection engines. To achieve such goal, it was first necessary to consolidate the methodology developed by the authors in the past for the simulation of the fuel-air mixing modeling [16, 17]. Since a correct prediction of the in-cylinder air-fuel ratio and trapped mass is crucial for a

successful combustion simulation, the attention was focused on different aspects, including:

- boundary and initial conditions setup to avoid the simulation of multiple cycles with late IVC engine operation;
- definition of suitable properties to describe the gasoline fuel, which is treated as a single component;
- description of liquid droplets phase change in presence of flash evaporation;
- wall film mass conservation.

The Weller model was chosen for the flame propagation prediction: it solves a transport equation for a combustion *regress* variable, *b*, and the reaction rate depends on the flame wrinkle factor Ξ. Using a regress variable ensures stability in the description of the flame propagation process and suitable expressions for Ξ can be directly taken from literature [18]. Transition from laminar to turbulent combustion is performed by means of a semi-empirical model derived from [19]. Tabulated kinetics was used for a correct estimation of the burned gas chemical composition. A look-up table, generated from homogeneous reactor auto-ignition calculations at constant pressure, was further processed to account for mixture fraction fluctuations according to a β-distribution. In this way, the effect of sub-grid mixture inhomogeneities is also considered. This work was carried out with the Lib-ICE code, which is based on the OpenFOAM technology and is extensively used for the simulation of both CI and SI engines for both research and industrial applications [20, 21].

Two different configurations were then selected to validate the proposed approach. The comprehensive database available in [22] was employed to validate the sub-model for the description of the laminar to turbulent flame propagation process. Experiments were carried out in a constant-volume vessel and the flame radius evolution was measured at different conditions of equivalence ratio, ambient pressure and turbulence intensity. After this first assessment, full-cycle simulations were carried out in a gasoline direct injection engine equipped with variable valve actuation. Three different operating points were considered with different speed and load and, for each condition, a detailed analysis of the computed results was carried out. Initially, the capability of the approach to correctly estimate the in-cylinder trapped air/fuel ratio and mass was evaluated. Afterwards, attention was focused on the engine combustion process. Comparison between computed and experimental data of in-cylinder pressure, heat release rate and pollutant emissions allowed a comprehensive evaluation of the proposed combustion model and to identify possible future necessary developments.

Numerical Models

Mesh Management

The full cycle simulation is carried out by employing a multiple number of automatically generated meshes [23]. Each mesh is generated for one specific crank angle and has a certain angular validity. Once a mesh is created, a Laplace equation is solved to accommodate the displacement of the internal mesh points from prescribed boundary motion. Eventually, the grid topology can be also modified applying suitable techniques, e.g dynamic mesh layering. When the *source* mesh quality is compromised by deformation, the computed flow field is interpolated in a newly created *target* mesh.

FIGURE 1 Automatic mesh generation process.

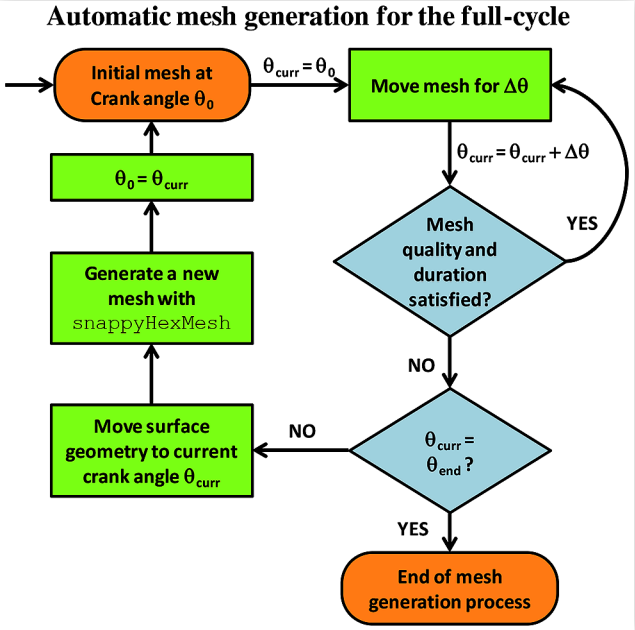

The Figure 1 summarizes the methodology adopted for the automatic mesh generation. Initially, the user has to provide a cleaned surface of the combustion chamber. A utility moves both piston and valves at positions corresponding to the crank angle where the simulation is started. At this stage, the mesh is automatically created using the Cartesian mesh generator snappyHexMesh available in the Open-FOAM code. Then the mesh is moved until duration, quality and validity criteria are satisfied. As soon as one of these fails, the engine surface geometry is moved to the current crank angle and a new mesh is generated. This process is sequentially performed until the end of the simulation is reached. At the end of the process, an entire set of meshes, satisfying the listed criteria, will be created and used for gas exchange, fuel-air mixing and combustion simulations.

Mesh deformation is used until the end of the intake stroke. To avoid that interpolation errors affect the simulation results during compression and flame propagation processes, the portion of the cycle from IVC to EVO is simulated using a single mesh whose topology is changed during the piston motion by means of the so-called *dynamic mesh layering* technique [24, 23].

Spray Model and Wall Film Model

The spray evolution is described by the Eulerian-Lagrangian approach, where computational parcels are introduced in the

CFD domain, each of them being representative of a set of identical droplets. Parcels evolve in the CFD domain according to the mass, momentum and energy exchange with the gas phase which is treated in a Eulerian manner. Specific sub-models are necessary to describe fuel evaporation, heat transfer, drag, breakup, collision and wall impingement. In the proposed approach, parcels are introduced in the computational domain with the same nozzle diameter and velocity resulting from injected mass flow rate and an expected area contraction coefficient. A short description of the spray model adopted in this work is presented there, and the reader is referred to [25, 17] for further details and a comprehensive validation. The injected particles mimic the liquid fuel jet and the Huh-Gosman model was applied to describe their atomization according to turbulent and aerodynamic instabilities [26]. Secondary parcels are formed because of mass stripping from the injected ones and they undergo further Kelvin-Helmholtz and Rayleigh Taylor breakup mechanisms [27]. Wall-impingement is handled by the Bai-Gosman model: depending on the Weber and Laplace impact numbers (We_i, La_i), four different regimes are identified and they are named *spread*, *stick*, *rebound* and *splash*. Only in the rebound regime there is no wall film deposition, while in the other tree the amount of momentum, mass and energy transferred to the liquid film depends on We_i and La_i. Compared to [25, 17], the methodology was slightly modified to improve the prediction of the fuel evaporation process. In past works, gasoline was assumed to be iso-octane, and the effect of fuel properties was not considered in detail since the attention was mainly focused on the correlation between spray targeting, mixture inhomogeneities and soot emissions. For a correct prediction of the combustion process, consistently with experimental data, the fuel must be completely evaporated and almost fully mixed with air at spark-timing. To achieve this, selection of numerical setup is first very important. Only second-order numerical schemes allow a correct description of the evolution of the in-cylinder charge motions, air entrainment by the spray and turbulence generation; the high numerical diffusivity induced by first-order numerical schemes might lead to an underestimation of the relative liquid gas velocity with corresponding low turbulence levels and evaporation rates. However, attention must be also focused on the fuel properties in the liquid phase. If fuel is approximated with iso-octane, evaporation can be slow and it can happen that there might be still some liquid fuel when combustion starts. Following [28], real gasoline properties as vapor pressure, latent heat, liquid viscosity were taken from [29] and implemented in OpenFOAM in a form of a table. The enthalpy, heat capacity and second virial coefficient of gasoline were assumed to be equal to the counterpart characteristics of n-octane. The critical temperature of gasoline was also taken from [29]. Gasoline density was implemented in a form of a table from [30]. Properties of gasoline vapor were approximated invoking the following mixing rule:

$$Q_m = \sum_{k=1}^{3} X_k Q_k \tag{1}$$

for a mixture composed by 15% of cyclo-hexane, 32% toluene and 55% iso-octane.

FIGURE 2 Comparison between iso-octane and the gasoline fuel properties: (a) Vapor pressure; (b) Density.

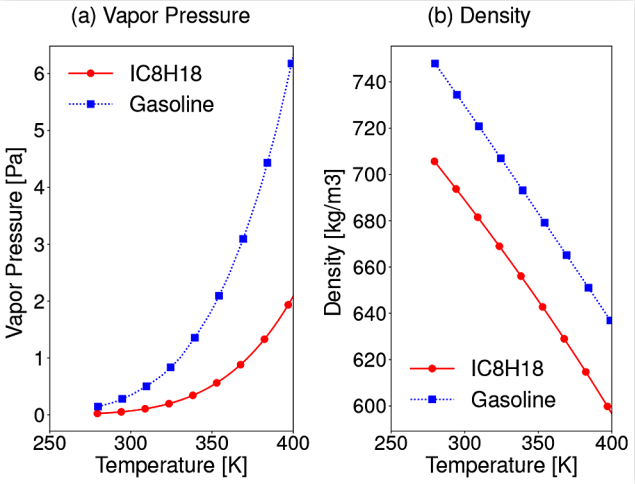

The Fig. 2(a)-(b) compare iso-octane and gasoline in terms of vapor pressure p_v and density ρ_l in the temperature range of interest for application to GDI engines. It is possible to see that the gasoline fuel has a higher density and this aspect corresponds to lower droplet velocities and, consequently, lower liquid penetration and tendency to impinge on the wall. The higher vapor pressure increases the evaporation rate and the mixture homogeneity at spark-timing.

If gasoline is used and the engine runs under the homogeneous operation mode, in the typical fuel injection rate of GDI engines (320-400 K), it is possible to see that p_v remains almost above the expected cylinder pressure during the injection phase. Which means that evaporation takes place under flash boiling conditions. This finding was also confirmed by [31] where optical investigations were carried out to characterize the morphology of gasoline and iso-octane sprays at pressure conditions which are similar to those encountered during the intake process. The Adachi model was used to describe flash evaporation in combination with modifications suggested by [32] to take also into account the effects of heat transfer inside the droplet. Such approach was previously applied by the authors for the simulation of hollow-cone sprays emerging from pressure swirl injectors [33].

To describe the impingement of the spray on the combustion chamber walls and its effect on the fuel-air mixing process, the liquid film model described in [34] was used in this work. The film moves on a curved wall surface, it has a variable thickness and assumed velocity profile, varying from zero at the wall to the free surface velocity. The film is assumed to be incompressible and moving with laminar flow. The Finite Area Method [34] was applied to solve the governing equations on the mesh boundary for liquid film volume, momentum and energy include the effects of spray impingement and film evaporation.

Ensuring the proper fuel mass balance inside the cylinder is of great importance for the simulation of GDI engines. At any time-step, the amount of injected mass must be equal to the sum of the corresponding spray, vapor and wall-film values. This aspect is made complex since wall film continuity

equation is solved for the film thickness and the liquid film density depends on temperature which is computed from the energy equation and depends on evaporation and heat transfer. Therefore, as soon as the film is formed and heated, there can be a loss of fuel mass which is nonphysical and only model-related. Under certain operating conditions characterized by significant impingement, the mass loss can be even higher than 10% which is not acceptable in case combustion and pollutant formation processes are intended to be simulated. To preserve the fuel mass balance, the wall film model was modified as follows:

- a global balance for the total wall film mass is performed considering the contributions from impingement and evaporation;
- the wall-film model solves for film thickness and computes the wall-film volume accordingly;
- the wall-film density is assumed to be constant in the whole domain and it is set to be equal to the ratio between the wall film mass computed from the global balance and the total film volume resulting from film thickness distribution;
- all the other film properties (heat capacity, thermal conductivity, viscosity, ...) depend on film temperature computed from the energy equation.

Combustion Model

Fig. 3 summarizes how the proposed methodology works for the prediction of combustion and, eventually, soot emissions. Transport equations are solved for mass, momentum, energy, turbulence, mixture fraction and its variance. Such quantities are used by the combustion model to compute the reaction rate in any computational cell. A lookup table provides the burned gas chemical composition from cell thermodynamic and mixing conditions including the mass fraction of soot precursors which can be eventually used by a semi-empirical model for the prediction of particle emissions.

FIGURE 3 Summary of the computational methodology to compute combustion and soot in gasoline, direct-injection engines.

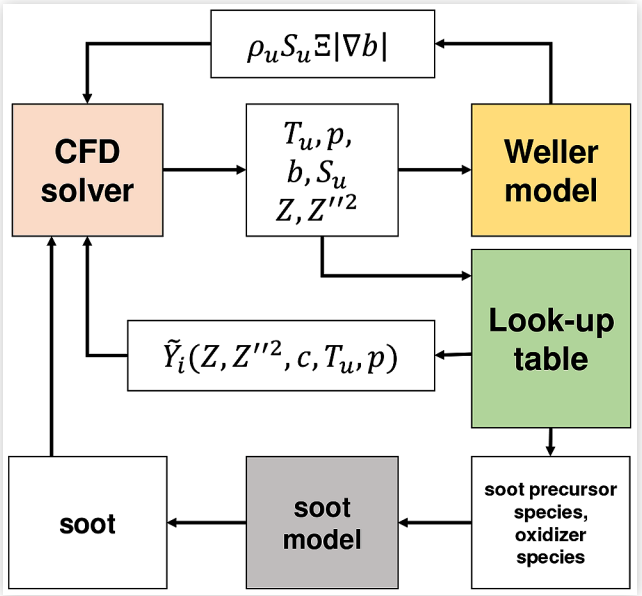

The Weller model is based on the laminar flamelet concept and describes the flame propagation by means of the unburned gas fraction b, known also as *regress* variable, and the flame wrinkle factor Ξ. The transport equation for b is [35, 36]:

$$\frac{\partial \rho \tilde{b}}{\partial t} + \nabla \cdot \left(\rho \tilde{\mathrm{U}} \tilde{b} \right) + \nabla \cdot \left(\mu_t \nabla \tilde{b} \right) = \rho_u \tilde{S}_u \tilde{\Xi} \left| \nabla \tilde{b} \right| + \dot{\omega}_{ign} \quad (2)$$

Eqn. 2 can be solved fully implicitly by exploiting differential operator properties. This ensures a stable solution for the flame propagation process even in presence of complex meshes and long time-steps. The ignition source term is represented by $\dot{\omega}_{ign}$ while $\rho_u \tilde{S}_u \tilde{\Xi} |\nabla \tilde{b}|$ is the reaction rate due to turbulent flame propagation. The flame wrinkle factor Ξ represents the ratio between turbulent and laminar flame speed S_t/S_u.

A simplified deposition model was used in this work [37] to describe the ignition process. The user specifies an initial flame kernel diameter d_k and time interval Δt_{ign}; in the cells whose distance from the spark plug is less than d_k an ignition source term is imposed:

$$\dot{\omega}_{ign} = \frac{C_s \rho_u b}{\Delta t_{ign}} \quad (3)$$

where C_s is a user-defined *strength* parameter, Δt_{ign} is the user-specified ignition duration and ρ_u is the unburned gas density. The regress variable distribution produced by the ignition model is suitable for the propagation of a premixed flame. However, it is necessary to find a proper expression for the flame wrinkle factor to account for the fact that the flame front is initially laminar and transition to fully turbulent flame propagation takes place only if the size of the flame kernel becomes comparable with the integral length scale [19]. The Ξ distribution in the CFD domain depends on the corresponding equilibrium value Ξ^* and on the regress variable b [36]:

$$\Xi = 1 + \left[1 + 2 \cdot S_\Xi \cdot (0.5 - b) \right] \cdot \left(\Xi^* - 1 \right) \quad (4)$$

In case $S_\Xi = 0$, flame wrinkling is uniform across the flame and its value corresponds to Ξ^*_{eq}. When $S_\Xi > 0$, it is assumed that the flame wrinkle factor grows across the flame. In this work, S_Ξ was set to 1, leading to:

$$\Xi = 1 \text{ if } b = 1 \quad (5)$$

$$\Xi = 2 \cdot \Xi^* - 1 \text{ if } b = 0 \quad (6)$$

Ξ^* is expressed as:

$$\Xi^* = f \cdot \Xi^*_{eq} \quad (7)$$

where the parameter f is used to describe the transition from laminar to turbulent flame. Following [19], f is computed as:

$$f = \left[1 - exp\left(-\frac{r_k}{\langle L_t \rangle} \right) \right]^{1/2} \cdot \left[1 - exp\left(-\frac{\langle u' \rangle + \langle S_u \rangle}{\langle L_t \rangle} \cdot t_{ign} \right) \right]^{1/2} \quad (8)$$

The expression $\langle\cdot\rangle$ denotes the average of a field around the spark plug in a volume with diameter $C_{vol}d_k$; L_t and u' are the turbulence intensity and integral length scale, respectively. t_{ign} is the time elapsed from spark timing and r_k is the flame kernel radius which is computed by a zero-dimensional model. Initially the flame is assumed to be laminar and r_k is computed from:

$$\frac{dr_k}{dt} = \frac{\rho_u}{\rho_b} I_{0,lam} S_u \tag{9}$$

and $I_{0,\,lam}$ is the laminar flame stretch parameter:

$$I_{0,lam} = \left(1.0 - \frac{\mathcal{L}_u \kappa}{S_u}\right) \tag{10}$$

where $\mathcal{L}_u$ is the Markstein length referred to the unburned gases. Assuming a spherical kernel, the strain rate κ is:

$$\kappa = \frac{2}{r}\frac{dr}{dt} \tag{11}$$

When the size of the kernel exceeds a multiple C_{Tay} of the Taylor turbulence micro-scale:

$$r_k = C_{Tay} \cdot \lambda = C_{Tay} \cdot \sqrt{10\nu \frac{k}{\varepsilon}} \tag{12}$$

dr_k/dt is computed assuming turbulent flame propagation and following [19]:

$$\frac{dr_k}{dt} = \frac{\langle \rho_u \rangle}{\langle \rho_b \rangle} \cdot \left[I_0 + I_0^{1/2} f \left(\langle \Xi \rangle - 1 \right) \right] \cdot \langle S_u \rangle \tag{13}$$

The expression for Ξ^*_{eq} is taken from Gulder [18]:

$$\Xi^*_{eq} = 1 + 0.62 \sqrt{\frac{u'}{S_u}} \mathcal{R}_\eta \tag{14}$$

where $\mathcal{R}_\eta$ is the Kolmogorov Reynolds number. During flame kernel growth, to ensure continuity in the dr_k/dt expression and both turbulence and laminar stretch effects, the expression for I_0 is computed as:

$$I_0 = min\left(I_{0,lam}, I_{0,turb}\right) \tag{15}$$

where the empirical relation from Bray [38] is used to estimate $I_{0,\,turb}$:

$$I_{0,turb} = \frac{0.117}{1+\tau} Ka^{-0.784} \tag{16}$$

where Ka is the Karlovitz number and $\tau = T_b/T_u - 1$.

The laminar flame correlation S_u employed in this work is computed using the Gulder correlation using the suggested coefficients for the iso-octane fuel.

Tabulated Kinetics

The chemical composition in any cell is computed from regress variable, mass fraction of chemical species in the burned and unburned state Y_b and Y_u, respectively.

$$Y_i = b \cdot Y_{u,i} + (1 - b) \cdot Y_{b,i} \tag{17}$$

FIGURE 4 Generation of the chemistry table used for the presumed PDF combustion model (TPPDF).

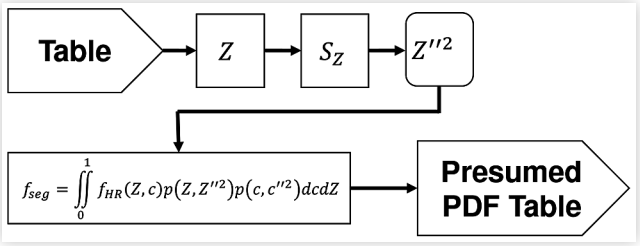

For a correct estimation of the soot precursor species even under expected homogeneous operation conditions, the burned gas chemical composition is computed from a lookup table which is based on homogeneous reactor, auto-ignition calculations and that is further processed to account for mixture fraction fluctuations. Hence, in any cell:

$$Y_b = Y_b\left(p, T_u, Z, \widetilde{Z''^2}\right) \tag{18}$$

where p is the pressure, T_u the unburned cell temperature, Z and $\widetilde{Z''^2}$ are mixture fraction and its variance, respectively. The methodology employed for the lookup table generation is illustrated in [39]. Fig. 4 illustrates how the homogeneous reactor table is processed to include the effects of turbulent mixture fraction fluctuations. The user specifies a range of mixture fraction segregation factor S_Z values, defined as the ratio between variance and maximum variance values:

$$S_Z = \frac{\widetilde{Z''^2}}{Z(1-Z)} \tag{19}$$

for any value of Z and S_Z it is possible to compute variances and the coefficients for the probability density function distributions. On the basis of them, integration is performed for all the tabulated quantities f_{HR} and a new table including the effects of mixture fraction fluctuation is available:

$$f_{seg} = \int_0^1 f_{HR}\left(p, T_u, Z, c\right) p\left(Z, \widetilde{Z''^2}\right) dZ \tag{20}$$

Inclusion of mixture fraction fluctuations will make soot prediction possible for GDI engines in operating conditions ranging from homogeneous to highly stratified conditions.

To correctly access to the lookup table, a transport equation is solved for the unburned gas enthalpy h_u which provides the fresh charge temperature T_u. Burned gas enthalpy h_b is estimated from h_u and the mean cell value:

$$h_b = \frac{h - b \cdot h_u}{1 - b} \tag{21}$$

accordingly, the burned gas temperature T_b is computed from h_b and composition $Y_{i,\,b}$.

Turbulence Model

CFD simulations were performed with the RANS approach, and the $k-\varepsilon$ model was used for turbulence with the suggested

literature standard coefficients. In particular, the C_1 constant was kept to 1.44 despite a higher value is generally suggested for a better prediction of jet penetrations [17]. A turbulent Schmidt number of 0.7 was considered in transport equations of regress variable, mixture fraction and its variance.

Constant-Volume Vessel Simulations

In [22], turbulent burning velocities of iso-octane air mixtures have been measured for expanding flame kernels within a turbulent combustion vessel. High speed Schlieren images were used to measure the flame radius evolution and derive the corresponding turbulent flame speed. Experiments were carried out including variation of ambient pressure (1-10 bar), turbulence intensity (0.5-6 m/s) and equivalence ratio (0.8-1.2) making possible to characterize the premixed combustion process under different conditions and producing a very useful database for combustion model validation. Initial vessel temperature is 360 K. Nine operating points were simulated, considering a stoichiometric mixture and three different pressure values. The reason for considering only a stoichiometric mixture was justified by the fact that engine simulations will be then performed only for homogeneous operation and equivalence ratio will not significantly vary inside the cylinder. Laminar flame properties are illustrated in Table 1 while details of the turbulent flow field are reported in Table 2. The main combustion model tuning constants are reported in Table 3.

TABLE 1 Laminar flame properties for the constant-volume vessel simulated conditions (p: pressure, ϕ: equivalence ratio; S_u: laminar flame speed; $\mathcal{L}_u$: Markstein length.

p [bar]	ϕ	S_u [m/s]	$\mathcal{L}_u$
1	1	0.51	3.1
5	1	0.30	0.5
10	1	0.25	0.2

TABLE 2 Detail of turbulent flow properties for the simulated operating conditions (u': turbulent intensity; p: ambient pressure; L: turbulent integral length; λ: Taylor scale; η: Kolmogorov scale).

Case	u' [m/s]	p [bar]	L [mm]	λ [mm]	η [mm]
1	1	1	20	2.6	0.12
2	4	1	20	1.3	0.042
3	0.5	5	20	1.6	0.060
4	1	5	20	1.2	0.035
5	4	5	20	0.58	0.012
6	6	5	20	0.47	0.0092
7	1	10	20	0.82	0.021
8	4	10	20	0.41	0.0074

TABLE 3 Combustion model tuning constants used for constant-volume vessel simulations.

C_Ξ	0.4
C_{Tay}	3
S_Ξ	

FIGURE 5 Constant-volume vessel simulated operating conditions reported on the Borghi diagram.

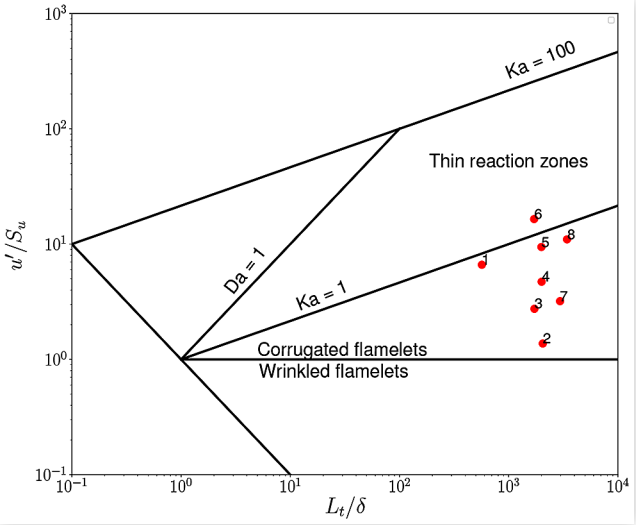

The Fig. 5 reports the simulated operating conditions on the Borghi diagram [40]. All the so-called *corrugated flamelets* regime is well covered. The ratio between turbulence intensity and laminar flame speed u'/S_u ranges from 1 to 10. The x-axis of the diagram reports the L_t/δ ratio where L_t is the turbulent integral length and δ is the laminar flame thickness. All the points have L_t/δ about 1000 except the operating point 1 where such ratio is slightly lower. The Markstein Lengths provided in [22] and displayed in Table 1 were used in the simulations for a correct estimation of the flame stretch.

Fig. 6 displays a comparison between computed and experimental evolution of the flame radius for the 1 bar initial vessel pressure. For the two different available values of the turbulence intensity (1 and 4 m/s), five different measurements were available. In both the conditions, the computed data slightly underestimate the experimental ones: mainly in the u'=1.0 m/s case it seems transition from laminar to turbulent flame is longer than what is reported in experiments. That point is characterized by the lowest L_t/δ ratio among the tested ones. Better results were achieved in the case of u'=4.0 m/s where computed flame radius is very close to the measured data and also transition to turbulent flame is clearly visible and happens at about 6 ms after the start of combustion.

The 5 bar ambient pressure condition is probably the one allowing the most comprehensive validation, since four different turbulence intensity values were considered. Increase of ambient pressure leads to a laminar flame speed reduction with condition 6 even crossing the boundary between corrugated flamelets and distributed reactions which is represented by Karlovitz number Ka = 1. A comparison between computed

FIGURE 6 Comparison between measured and computed flame radius at initial vessel temperature T = 360 K and pressure p = 5 bar: (a) u' = 1.0*m/s*; (b) u' = 4.0*m/s*.

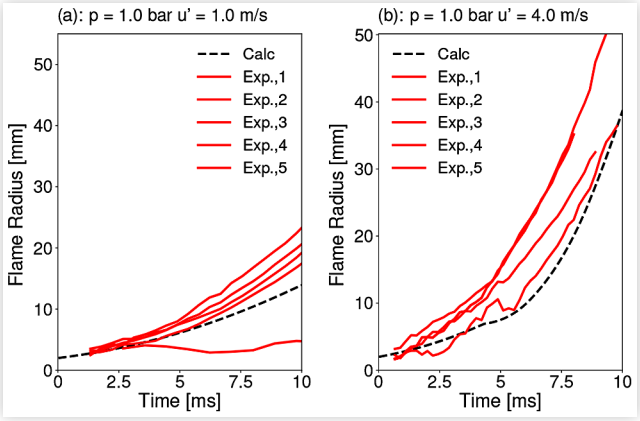

FIGURE 8 Comparison between measured and computed flame radius at initial vessel temperature T = 360 K and pressure p = 10 bar: (a) u' = 1.0*m/s*; (b) u' = 4.0*m/s*

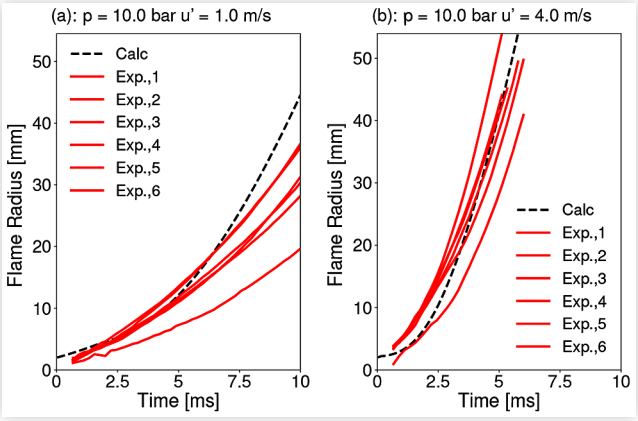

and experimental results is provided in Fig. 7 where it is possible to see that model predictions always fall within the expected experimental range. Flame speed increases with turbulence intensity and this aspect is well-captured by the adopted Gulder's formulation illustrated in Eqn. 14.

For the sake of completeness, results for the two tested conditions at 10 bar are also reported in Fig. 8. Computed flame radius evolution is still in rather good agreement with experimental data, despite a slight overestimation for the lowest turbulence intensity condition. Model assessment with constant-volume vessel data illustrate that the proposed approach to model combustion in spark-ignition engine is capable to correctly reproduce the initial flame propagation process including also the transition to fully turbulent combustion. The use of experimental data from [22] was of great importance since they allowed a validation of model under well-defined ambient and turbulence intensity conditions without the additional complexity which is generally introduced in engine simulations by charge motions, mixture formation and heat transfer.

FIGURE 7 Comparison between measured and computed flame radius at initial vessel temperature T = 360 K and pressure p = 1 bar: (a) u' = 0.5*m/s*; (b) u' = 1.0*m/s*; (c) u' = 4.0*m/s*; (d) u' = 6.0*m/s*

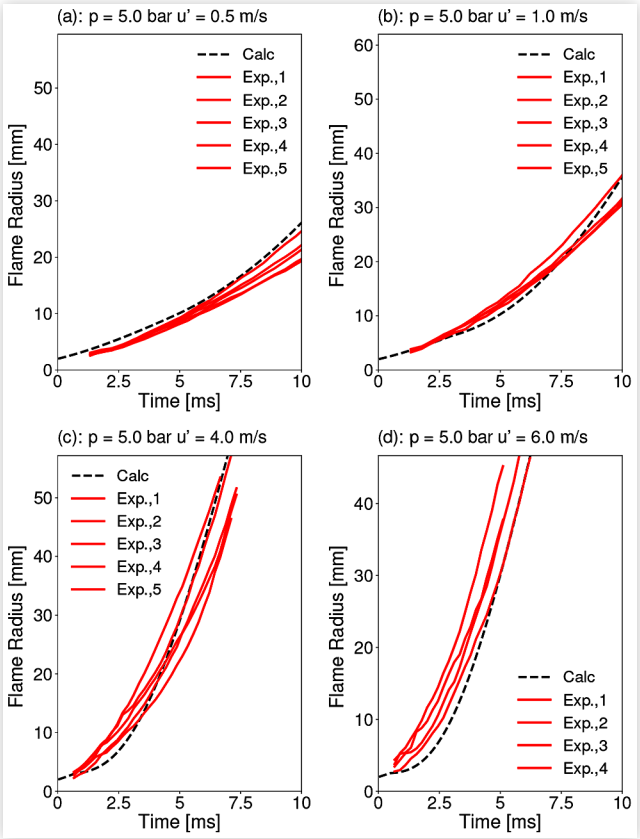

GDI Engine Simulations

Engine Description and Simulated Operating Points

To validate the comprehensive methodology for the simulation of gas exchange, fuel-air mixing and combustion in SI engines, full-cycle simulations were carried out in a three cylinder, turbocharged engine with variable valve actuation. The main engine geometry data are reported in Table 4

Table 5 reports the main details of the simulated operating conditions in terms of engine speed, load (bmep), air/fuel ratio, injection pressure, intake valve timing (IVO and IVC) and valve lift, normalized with respect to the maximum value l/l_{max} . The first operating point illustrates that load control is mainly achieved by variable valve actuation making

TABLE 4 Main geometry data of the simulated gasoline direct-injection engine.

Bore	~ 70 mm
Stroke	~ 85 mm
Compression ratio	~ 13

TABLE 5 Details of the simulated operating conditions: engine speed, bmep, air/fuel ratio, injection pressure, valve timing (IVO and IVC), valve lift *l* normalized with respect to the maximum allowed engine value l_{max}.

Condition	2000x2	4000x17	5500-Full
Speed [rpm]	2000	4000	5500
bmep [bar]	2	17	16
Air/fuel ratio	14.5	14.5	14.5
Injection pressure [bar]	50	180	200
IVO [deg ATDC]	0	-10	-10
IVC [deg BTDC]	270	70	70
l/l_{max}	0.4	1	1

possible to reduce the pumping losses: the 2 bar bmep is achieved by short valve opening duration combined with a reduced lift. The two other operating points have similar load, different speeds and they are both characterized by Miller cycle operation with late intake valve closure.

CFD Simulation Setup

Details of the computational mesh are reported in Fig. 9. The mesh size is 1 mm in most of the cylinder, except for a cone region where the spray is expected to evolve where it was reduced to 0.5 mm. One boundary layer was placed on the valve and cylinder head surfaces while three were used on the liner. For all the cylinder patches, mesh size was set to 0.5 mm except for the valve seat and in the crevices where resolution was reduced to 0.125 mm.

All the simulations start from EVO and the computational domain initially includes cylinder, intake and exhaust ports. The intake port must be present in the CFD domain from the beginning of the simulation since the proper flow-field must be established inside it before IVO for a correct prediction of the trapped in-cylinder mass. At simulation start time, no flow is assumed and different values of pressure, temperature and composition are imposed at intake, exhaust and cylinder domains. Data from one-dimensional simulation of the whole engine system were used to initialize pressure and temperature in the computational domain and as unsteady boundary conditions in the inlet and outlet boundary. Initial cylinder and exhaust port chemical composition corresponds to complete fuel oxidation according to the specified air/fuel ratio. Composition boundary conditions at the inlet port are more complex to be imposed since there might be a significant amount of fresh charge that flows back to the intake manifold due to operation with late inlet valve closing.

FIGURE 9 In-cylinder mesh structure and size in the different regions.

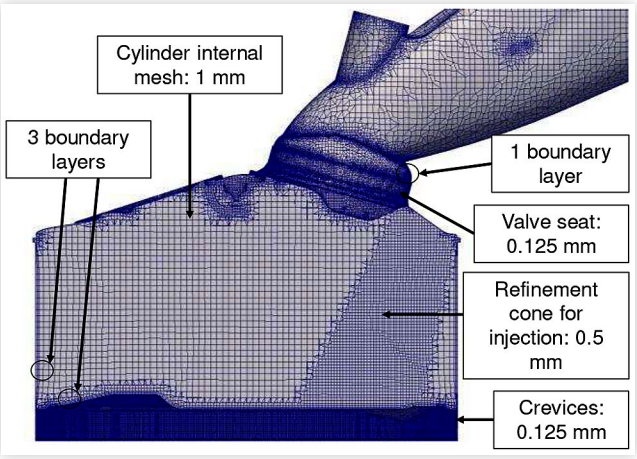

If it is assumed that there is only air in the intake manifold at the beginning of the calculation, at least two cycles have to be simulated for a correct prediction of the trapped air/fuel ratio. To reduce the computational time and perform only a single cycle simulation, 1D data of mass flow across the inlet valve and inlet port were processed to determine the amount of lost fresh charge and incoming in-cylinder air. From this mass balance it was possible to compute the corresponding fuel mass fraction at the inlet boundary which was then imposed as boundary condition. Fig. 10(a)-(b) report the mass flow rate of air and fuel across the inlet valves for one of the simulated operating points. After BDC (540), it can be clearly seen that fresh charge (air and fuel) leaves the cylinder.

To compute the fuel mass fraction to be imposed at the inlet boundary to avoid the simulation of the second cycle, it is assumed that:

- All the fresh charge mass lost (m_{lost}) due to backflow comes back to the cylinder at the next cycle. The air/fuel ratio of m_{lost} is equal to the nominal value for the considered operating point.
- The rest of the incoming cylinder mass is only pure air (m_{air})

To ensure the correct air/fuel ratio, the fuel mass fraction to be imposed at the inlet boundary must be:

$$y_{fuel} = \frac{m_{lost} \cdot \left(\frac{A}{F}\right)}{m_{lost} + m_{air}} \tag{22}$$

Further information related to the CFD setup for the three selected operating points is reported in Table 6. The maximum mesh size is about 2 million cells, which was reached during the overlap phase for the 4000x17 and 5500-Full conditions. The number of meshes required to complete the gas exchange process from EVO to IVC ranges from 80 to 90 mainly depending on the duration of the valve overlap period. Since it is not possible to simulate the contact between the poppet and seat surface, the valve is assumed to be closed when its lift is lower than 0.25 mm. At that instant, the port domain is physically detached from the cylinder one. Simulations were carried out on 28 core machine with Intel(R) Xeon(R) CPU E5-2690 v4 processor with 2.60GHz.

Gas Exchange and Fuel-Air Mixing Simulations

Fig. 11(a)-(b) compare computed in-cylinder pressure with the experimental data and 1D simulation results for a crank

FIGURE 10 (a) in-cylinder air and fuel mass flow rates across the inlet valves; (b) mass lost because of backflow and mass of fresh air entering in the cylinder for any cycle.

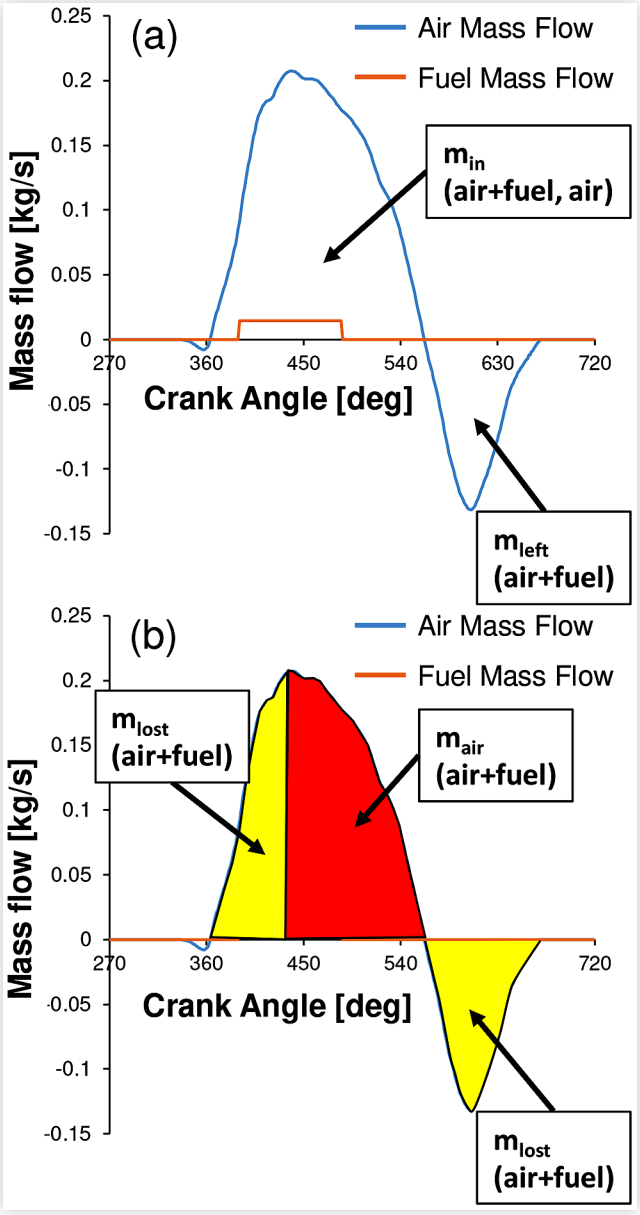

TABLE 6 Details of the simulation setup for the three selected operating points.

Condition	2000x2	4000x17	5500-Full
Meshes	83	92	88
Time-step [CAD]	0.05	0.05	0.05
CPU time [days]	5.5 days	5 days	5 days

angle interval ranging from TDC during gas exchange up to IVC for the 2000x2 and 4000x17 conditions, respectively. The 5500-Full operating point is not reported since its main features are very similar to the 4000x17 one. Consistently with the origin of imposed inlet and outlet boundary conditions,

FIGURE 11 Comparison between computed in-cylinder pressure with experimental data and 1D simulation results. (a) 2000x2 condition; (b) 4000x17 condition.

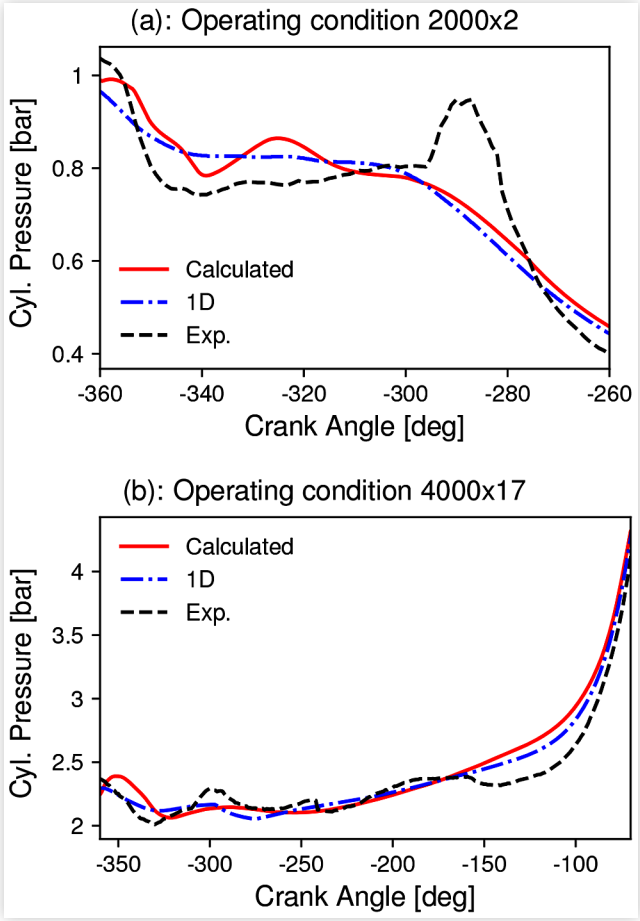

CFD cylinder pressure is in rather good agreement with 1D data. However, in 2000x2 condition there is a significant discrepancy between the computed and experimental profiles: in the second part of the intake phase, measured pressure trace shows a local peak which is not predicted correctly by the 1D and CFD simulations.

The evolution of the fuel mass in the computational domain is reported in Fig. 12(a)-(b). For both the analyzed conditions, the history of liquid fuel, evaporated, wall film and injected fuel mass is reported. For the sake of consistency, Fig. 12(a)-(b) also display the total fuel mass in the CFD domain. In the 2000x2 operating condition, valve closes before BDC. Hence there is no backflow from the cylinder to the intake port and, when injection starts, the fuel mass in the CFD domain is zero. Very low cylinder pressure promote flash evaporation and a very small amount of wall film is formed. All the fuel is completely evaporated at about 200 CAD BTDC and it expected to have enough time to mix with the surrounding air for an efficient combustion process. Interpolation errors due to solution mapping are below 0.3% in this case which can be considered to be acceptable. The other two operating conditions are characterized by late IVC and, because of charge backflow, fuel is already present in the intake port when injection starts. The IVC timing can

FIGURE 12 Evolution of fuel mass inside the computational domain distributed between liquid spray, vapor and wall film. (a) 2000x2 condition; (b) 4000x17 condition.

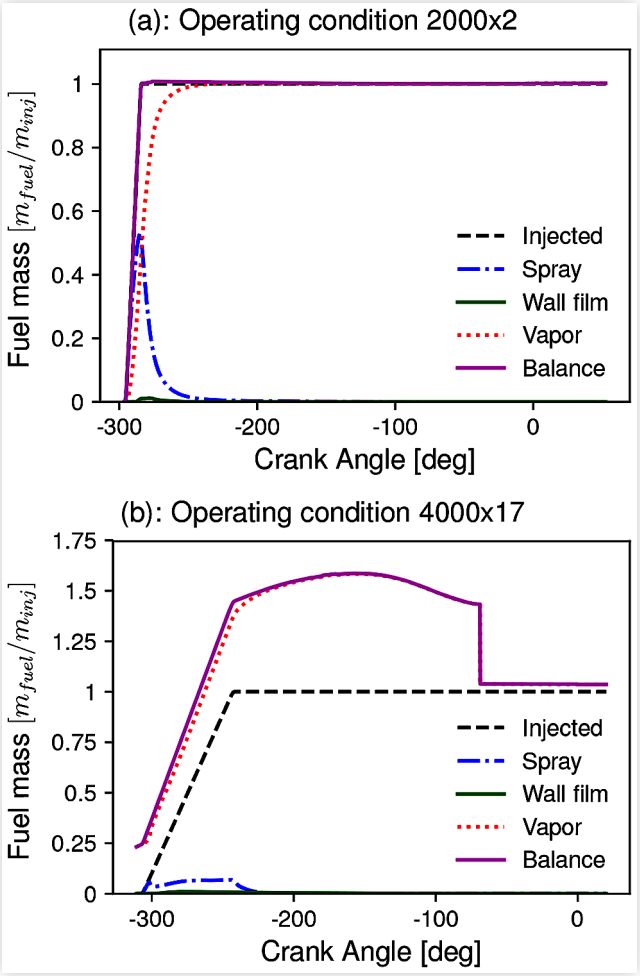

be clearly distinguished as the moment in which the total amount of fuel drops down due to the removal of the intake port from the CFD domain.

However, both in the 4000x17 and 5500-Full conditions, the amount of fuel inside the cylinder is higher than the corresponding injected one. Authors have first verified that, even in this cases, mapping errors do not affect the amount of fuel mass inside the cylinder. Hence, such discrepancy can be related to:

- simulated IVC timing which is generally anticipated with respect to the experimental one due to the assumption that valve is closed when its lift is lower than 0.25
- adopted method for inlet fuel boundary conditions
- imposed 1D boundary conditions
- predicted valve flow coefficient across the intake valves

Fig. 12(b) can be helpful to understand how the selected minimum valve lift value affects the trapped in-cylinder fuel mass: it is possible to clearly identify the effect of backflow after the BDC since the amount of fuel inside the computational domain is being reduced. Right before the IVC, the amount of fuel mass inside the computational domain clearly reaches a local minimum which shows that the backflow process is almost terminated. Any further reduction of the valve lift will not produce a relevant reduction of the fuel mass inside the computational domain.

FIGURE 13 Evolution of trapped in-cylinder air/fuel ratio for the three simulated operating points.

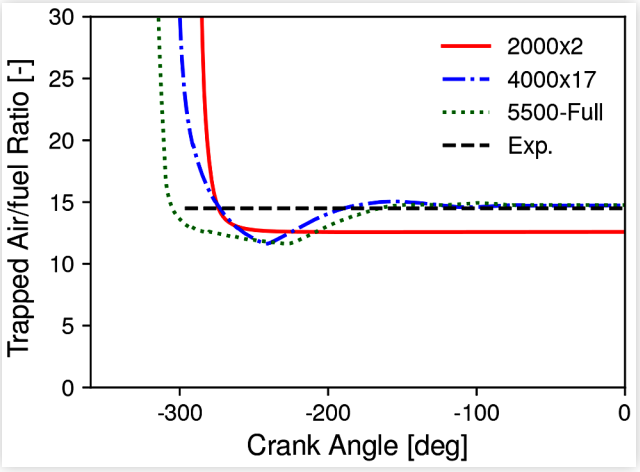

To understand if the discrepancy is related to the method employed for inlet fuel mass fraction initial and boundary conditions, Fig. 13 illustrates the evolution of the trapped in-cylinder air/fuel ratio for the three simulated operating points. Results are satisfactory for the 4000x17 and 5500-Full conditions, while there is a clear underestimation in the 2000x2 case: computed equivalence ratio ϕ is about 1.15 against the expected experimental $\phi = 1$ value. Focusing on the high load cases, they are both characterized by long valve opening periods combined with high lifts: the air-fuel ratio is correctly estimated but the trapped fuel mass is overpredicted. Such result suggests that the imposed initial and boundary conditions for the fuel mass are correct and that the origin of the discrepancy is mainly in the backflow process: the CFD simulation probably estimates a valve reverse flow coefficient which is lower than the value adopted in 1D simulations. Pressure boundary conditions at the inlet port are the reason for the underestimated in-cylinder air mass: the one-dimensional code does not predict any pressure peak in the intake system and this negatively affects the predicted in-cylinder mass. Considering the already very good agreement between 1D and CFD in-cylinder pressure trends, authors do not think that multi-cycle simulation can significantly improve the computed results for the gas exchange process in terms of trapped fuel and air mass for the high and low load cases, respectively. The increasing engine complexity related to the use of turbocharging, direct-injection, VVA and late IVC timing probably introduces also new challenges for 1D engine modeling which should be properly addressed for a better prediction of the engine performance and to provide accurate boundary conditions for the CFD simulations.

Fig. 14(a)-(b) illustrate that the valve timing and engine load strongly affect the in-cylinder tumble and the related generation of in-cylinder turbulence which was here

FIGURE 14 (a) Computed evolution of in-cylinder tumble ratio during intake and compression phases for the three simulated operating conditions; (b) Computed evolution of in-cylinder turbulence intensity normalized by the mean piston speed during intake and compression phases for the three simulated operating conditions.

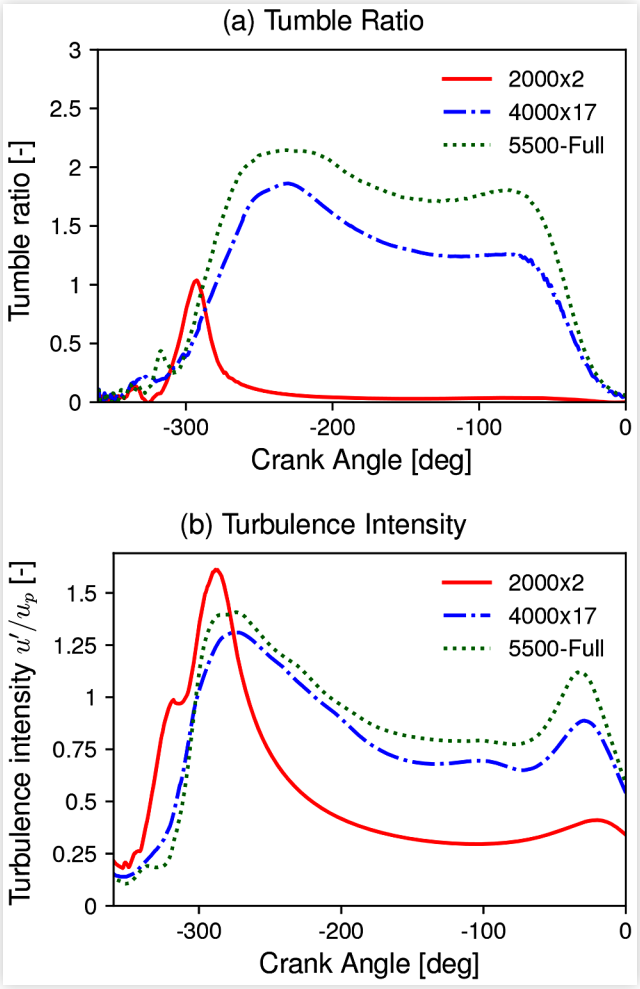

normalized by the mean piston speed. Full load cases have very similar values of the tumble ratio during the intake phase and turbulence intensity seems to scale rather well with the piston speed. Early IVC is the responsible of very low turbulence levels for the 2000x2 condition.

To complete the analysis on the fuel-air mixing process, the distribution of the relative air-fuel ratio at spark-timing is reported in Fig. 15(a)-(b). High engine load and speeds makes the mixture very homogeneous in the 4000x17 and 5500-Full operating points. Initially, all the three simulations were performed considering a uniform initial jet angle of 16 degrees. However, such value did not produce an ignitable mixture at spark-timing in the 2000x2 condition, where it is possible to see in Fig. 15 that reduced in-cylinder turbulence and charge motions makes the mixture very inhomogeneous. The mixture becomes ignitable when increasing the cone-angle to 30 deg. Such modification is justified by the fact that strong flash evaporation conditions enlarges the spray angle

FIGURE 15 ((a) Distribution of the relative air-fuel ratio at spark-timing for the 4000x17 and 5500-Full conditions; (b) Effect of the spray cone angle on the relative air-fuel ratio distribution for the 2000x2 operating condition.

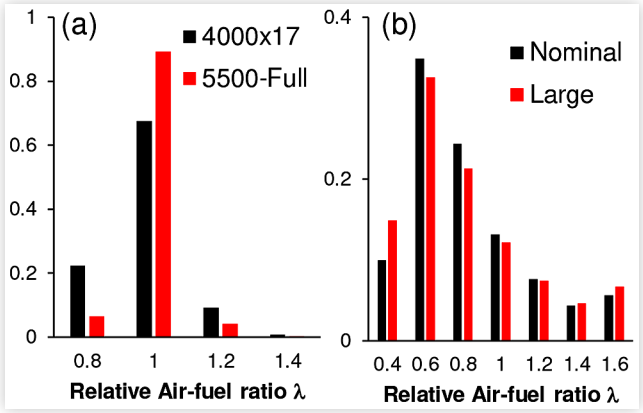

FIGURE 16 Effect of initial spray cone angle on the in-cylinder droplet distribution during the intake stroke for the 2000x2 operating condition. Droplet color scale: red (max diameter) to blue (min diameter).

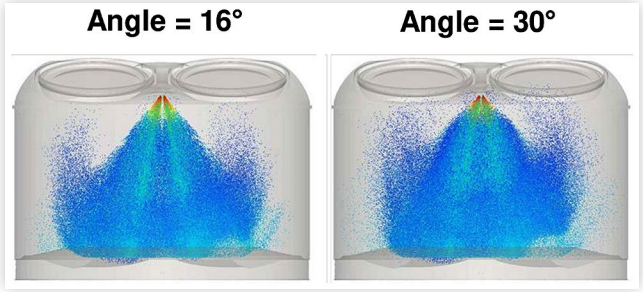

due to the ejection of small droplets from the liquid core, as discussed in [32, 41].

For the sake of completeness, the effect of spray cone angle for the 2000x2 is presented in Fig. 16 where droplet distribution in the computational domain is shown halfway during the intake stroke. The spray collapse due to the flash boiling is further increased with 30 degree jet angle and this produces a reduced penetration with a higher fuel concentration near the cylinder axis.

Combustion Simulations

The simulation of compression, combustion and expansion phases was carried out with a single mesh, whose topology was modified by adding and removing cell layer close to the piston boundary. The total number of cells is about 500000 at TDC. The combustion model tuning constants are reported in Table 7: compared to vessel simulation, C_{Ξ} was slightly increased while the Taylor scale multiplier reduced. The same set of constants was used for the simulation of all the three operating points. In the proposed model, the zero-dimensional approach for the computation of the flame radius is mainly used to estimate the transition from laminar to

TABLE 7 Combustion model tuning constants for engine simulations.

	C_s	Δt_{ign}	C_Ξ	C_{vol}	C_{Tay}	t_{spk}
2000x2	6	1.2	0.45	10	1	-41.5
4000x17	2	0.4	0.45	10	1	-2.5
5500-Full	2	0.4	0.45	10	1	1.5

FIGURE 17 Computational mesh used for combustion simulations in the GDI engine.

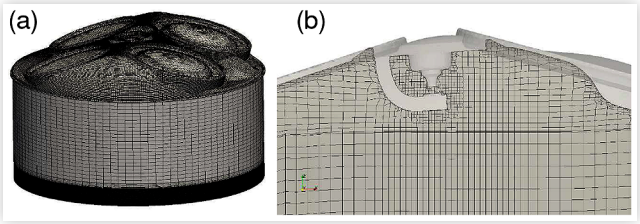

turbulent flame propagation. However, the tuning of the ignition model is very important to generate a stable flame kernel and allow flame propagation in the computational domain. The main parameters C_s, Δt_{ign} and d_k were selected to ensure the formation of a stable and relatively small and stable kernel where the regress variable b reaches the zero value and prevents it to increase because of turbulent diffusion when ignition is terminated. This is generally achieved by selecting a relatively small value of d_k combined with a high C_s value. This ensures a correct propagation of the flame from $b = 0$ to $b = 1$ and avoids any significant influence of the ignition model on the heat release rate profile. A longer duration of the ignition phase was selected for the 2000x2 condition due to the lower mixture ignitability related to the presence of low turbulence and high charge inhomogeneity. Nevertheless, the same intensity for ignition was used, since the $\frac{C_s}{\Delta t_{ign}}$ ratio was kept constant. With respect to gas exchange simulations, the in-cylinder temperature, pressure and mixture fraction fields were slightly scaled to match the experimental amount of trapped air mass for a correct estimation of the cumulative heat released by combustion. A slight overestimation, about 3% was found for the 4000x17 and 5500-Full conditions. An underestimation of about 15% of the trapped air mass was found instead for the 2000x2 case.

The air/fuel mixture distribution at spark-timing for the 2000x2 operating condition is reported in Fig. 18. Consistently with Fig. 15(b), it is possible to see that the mixture is not homogeneous inside the cylinder and the fuel mass fraction increases with the distance from the spark-plug. This aspect, combined with the low in-cylinder turbulence related to the very early IVC timing, is one of the reasons of a rather long combustion duration for this condition. The fuel mass fraction in Fig. 18 is reported on the cylinder symmetry plane. Another plane is also shown in the same figure and it will be used to visualize the temperature field during the combustion process.

Fig. 19 illustrates the flame development from the side and top views of the combustion chamber: temperature field and regress variable $b = 0.5$ iso-surfaces are reported. Despite

FIGURE 18 Computed fuel mass fraction distribution at spark-timing for the 2000x2 operating conditions.

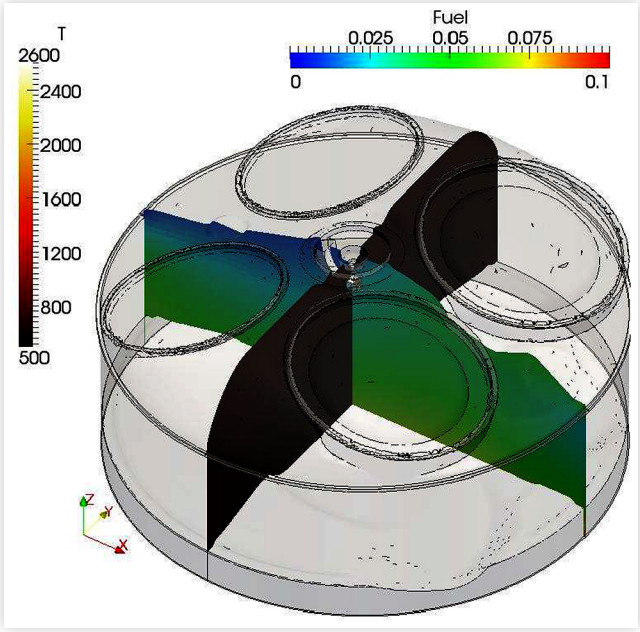

FIGURE 19 Flame propagation process as function of crank angle for the 2000x2 operating condition. On the top of each sub-figure temperature field is visualized on a plane located between intake and exhaust valves and passing through the center of the spark plug. On the bottom of each sub-figure the flame is represented as b = 0.5 iso-surface.

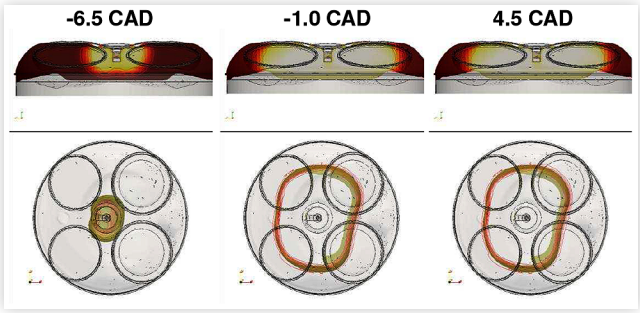

very early spark-timing, lean mixture close to the spark-plug and low in-cylinder turbulence are the reasons of a very slow flame propagation process: the flame front becomes clearly visible just 6.5 CAD BTDC. The model capability to describe the combustion process is displayed in Fig. 20, reporting a comparison between computed and experimental values of in-cylinder pressure and apparent heat release rate (AHRR) profiles. The peak-pressure location is correctly estimated despite an underprediction of the peak value. Such condition is particularly demanding for the combustion model, since the turbulence at spark-timing is very low. Two possible reasons can be found for such discrepancy: first, turbulence can be too low because of the underestimation (about 10%) of the trapped air mass. Another possible explanation can be related to the adopted combustion model which is not

FIGURE 20 Combustion model validation for the 2000x2 operating point: comparison between computed and experimental in-cylinder pressure and apparent heat release rate profiles.

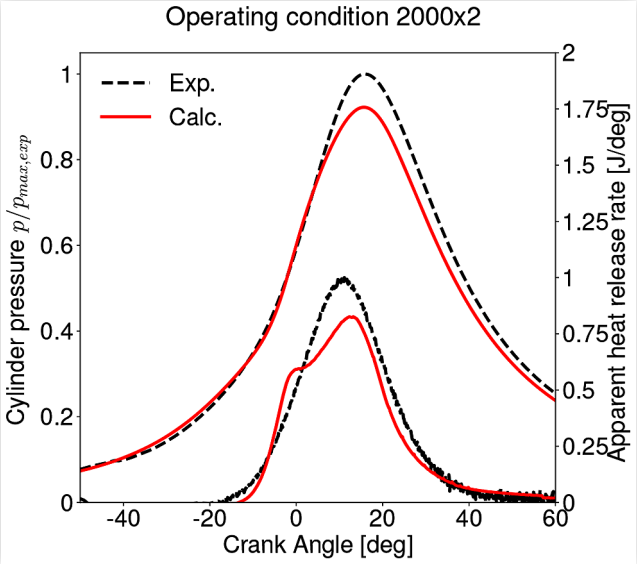

capable to generate enough turbulence across the flame front. Preliminary results performed with higher intake pressure boundary condition to better match the experimental air/fuel ratio do not produce any significant improvement to the computed cylinder pressure trace and, for this reason, more investigations are probably necessary for the combustion model.

Compared to the 2000x2 condition, the 4000x17 is characterized by intake valve closing time taking place almost halfway the compression stroke. Valves are open for the whole intake stroke and this aspect enhances the mixing between fuel and air: Fig. 15(a) shows that at spark-timing the fuel-air mixture is nearly homogeneous. Moreover, all the tumble motion was converted into turbulent kinetic energy towards the end of the compression stroke. The consequence is a nearly cylindrical flame shape, centered around the spark-plug, as it is illustrated in Fig. 21.

Spark timing for the 4000x17 condition happens at 2.5 CAD BTDC and combustion mainly develops after the top dead center. Turbulence is already decaying and this condition is surely demanding for the combustion model which should be able to describe, mainly in the initial stage, the flame propagation process with continuous reduction of the turbulence intensity. Fig. 22 compares measured and calculated in-cylinder pressure and heat release rate profiles for the 4000x17 operating condition. Simulation correctly predicts the effective time at which combustion starts, about 4 CAD after TDC. Computed apparent heat release profile overestimate the experimental value until the pressure peak is reached, afterwards the burnout phase seems to be rather well predicted by the model, after 20 CAD ATDC. Overestimation of AHRR produces a higher computed pressure peak compared to experimental data. Some investigations were performed to understand the origin of such discrepancy because, qualitatively, the shape of the AHRR profile looks also similar to those of the 2000x2 condition. A clear inflection can

FIGURE 21 Flame propagation process as function of crank angle for the 4000x17 operating condition. On the top of each sub-figure temperature field is visualized on a plane located between intake and exhaust valves and passing through the center of the spark plug. On the bottom of each sub-figure the flame is represented as b = 0.5 iso-surface.

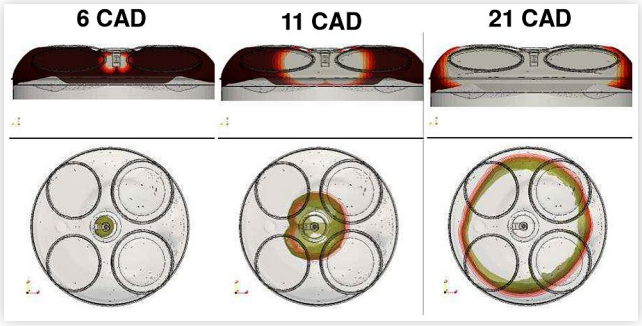

FIGURE 22 Combustion model validation for the 4000x17 operating point: comparison between computed and experimental in-cylinder pressure and apparent heat release rate profiles.

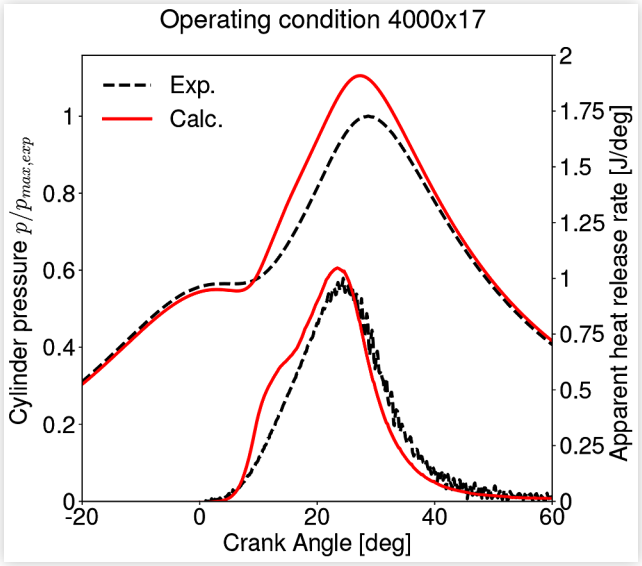

be observed in the phase where apparent heat release is growing. The reason for that seems to be the predicted turbulence intensity distribution inside the cylinder, which is not completely symmetrical and slowing down the flame speed. Experimental data probably reveals a more homogeneous turbulence distribution. More investigations are required to improve this result, including also a detailed investigation about the effect of the spray evolution on in-cylinder charge motion. All the simulations were run here with the standard $k-\varepsilon$ model for turbulence, with the C_1 constant set to 1.44. In Diesel spray simulations, such value is generally increased up to 1.55 to better describe the jet penetration and this different setup might affect both mixture and turbulence distribution.

FIGURE 23 Combustion model validation for the 5500-Full operating point: comparison between computed and experimental in-cylinder pressure and apparent heat release rate profiles.

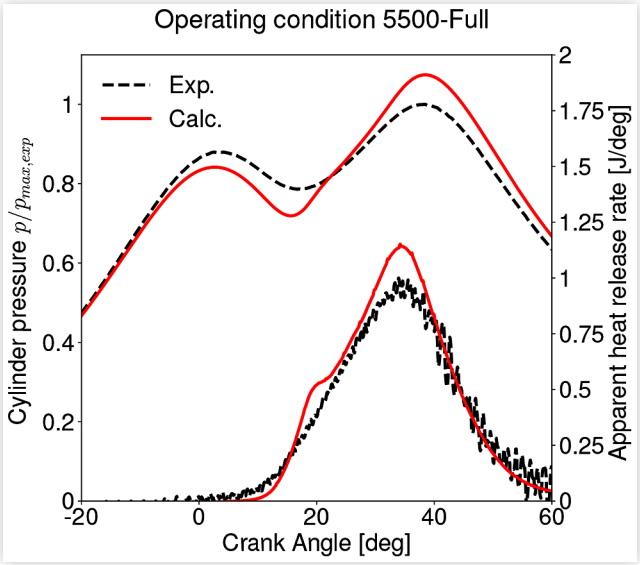

For the sake of completeness, Fig. 23 reports the results for the 5500-Full condition: they are very similar to those of 4000x17 one and this aspect can be clearly justified by the fact that both conditions have very similar levels of turbulence intensity and mixture homogeneity. Also in this case cylinder pressure is overpredicted because of the too fast release of heat in the first part of the combustion process. For sure results can be improved for the 4000x17 and 5500-Full conditions by reducing the C_{Ξ} model constant, but this aspect will negatively affect the results of the 2000x2 condition making computed cylinder pressure trace further underestimated.

Conclusions

This work was focused on simulation of the full cycle process, including combustion, in a gasoline direct-injection engine. The selected configuration is well representative of the current and future generation of SI engines and is very challenging for CFD modeling, since the use of VVA and non conventional IVC timing requires accurate boundary and initial conditions for a correct estimation of the trapped in-cylinder air/fuel ratio, charge motions and turbulence intensity. The Weller approach was selected to predict the combustion process: an algebraic expression was used to compute the flame wrinkle factor together with a quasi-dimensional model to describe the transition from laminar to turbulent flame propagation. The validity of the combustion model was first verified using constant-volume combustion vessel data, under controlled ambient and turbulence conditions. Pressure and turbulence intensity effects are rather well described, showing that the expressions used for turbulent to laminar flame speed [18] and for transition from laminar to turbulent flame propagation [19] are valid for the expected combustion regimes encountered in spark-ignition engines. Such preliminary validation of the combustion model was of great help to better understand its performance when applied to real engine configurations. Gas exchange and fuel-air mixing simulations mainly illustrated how in-cylinder air/fuel ratio is affected by the accuracy of 1D boundary conditions, suggesting that further efforts are required for what concerns one-dimensional engine modeling for a better description of the pressure wave motion in the intake manifolds. Moreover, operation under early/late IVC requires probably to focus more the attention on the valve flow coefficients adopted by the 1D model and the ones predicted during the CFD simulation. The proposed methodology for the simulation of the fuel-air mixing process is conservative with respect to the fuel mass balance and can produce an ignitable mixture at spark-timing consistently with the real engine operation. Inclusion of flash evaporation and real gasoline properties increase the evaporation rate and reduces the charge inhomogeneities compared to the case where iso-octane is adopted. These prerequisites are fundamental for a successful simulation of the flame propagation process, making possible to estimate engine performance and emissions. Satisfactory results were achieved for what concerned the simulation of the combustion process since all them were achieved without changing the main model tuning constants. The proposed model is capable to reproduce the experimental cylinder pressure trace under very demanding conditions:

- very low load conditions where a very long transition from laminar to turbulent flame propagation;
- high load in presence of delayed spark timing where the flame propagation process happens in presence of strongly decaying turbulence.

The combustion model is very sensitive to the in-cylinder turbulence levels and its distribution within the combustion chamber. For this reason it is probably necessary to improve the prediction of the interaction of in-cylinder charge motions and its interaction with the injected fuel spray. Such topic will be matter of future investigations together with the prediction of soot and NO_x emissions.

Acknowledgment

This paper is supported by European Union's Horizon 2020 research and innovation programme under grant agreement no. 724036, project UPGRADE.

References

1. Lemazurier, L., Shidore, N., Kim, N., Moawad, A. et al., "Impact of Advanced Engine and Powertrain Technologies on Engine Operation and Fuel Consumption for Future Vehicles," SAE Technical Paper 2015-01-0978, 2015, doi:10.4271/2015-01-0978.
2. Kalghatgi, G. T., "The Outlook for Fuels for Internal Combustion Engines," *International Journal of Engine Research* 15(4):383-398, 2014.

3. Johnson, T., "Vehicular Emissions in Review," *SAE Int. J. Engines* 9(2):1258-1275, 2016, doi:10.4271/2016-01-0919.
4. Lavoie, G. A., Ortiz-Soto, E., Babajimopoulos, A., Martz, J. B., and Assanis, D. N., "Thermodynamic Sweet Spot for High Efficiency, Dilute, Boosted Gasoline Engines," *International Journal of Engine Research* 14(3):260-278, 2013.
5. Chang, J., Viollet, Y., Alzubail, A., Abdul-Manan, A. F. N., and Al Arfaj, A., "Octane-on-Demand as an Enabler for Highly Efficient Spark Ignition Engines and Greenhouse Gas Emissions Improvement," SAE Technical Paper 2015-01-1264, 2015, doi:10.4271/2015-01-1264.
6. Bonandrini, G., Di Gioia, R., Papaleo, D., and Venturoli, L., "Numerical Study on Multiple Injection Strategies in DISI Engines for Particulate Emission Control," SAE Technical Paper 2012-01-0400, 2012, doi:10.4271/2012-01-0400.
7. Bozza, F., De Bellis, V., and Teodosio, L., "Potentials of Cooled EGR and Water Injection for Knock Resistance and Fuel Consumption Improvements of Gasoline Engines," *Applied Energy* 169:112-125, 2016.
8. Toulson, E., Schock, H. J., and Attard, W. P., "A Review of Pre-Chamber Initiated Jet Ignition Combustion Systems," SAE Technical Paper 2010-01-2263, 2010, doi:10.4271/2010-01-2263.
9. Hong, H., Parvate-Patil, G. B., and Gordon, B., "Review and Analysis of Variable Valve Timing Strategies - Eight Ways to Approach," *Proceedings of the Institution of Mechanical Engineers, Part D: Journal of Automobile Engineering* 218(10):1179-1200, 2004.
10. Fontana, G., Galloni, E., and Torella, E., "Experimental and Numerical Analysis of a Small VVT S.I. Engine," SAE Technical Paper 2005-24-079, 2005, doi:10.4271/2005-24-079.
11. Duclos, J. M. and Colin, O., "Arc and Kernel Tracking Ignition Model for 3D Spark-Ignition Engine Calculations," in *Proceedings of COMODIA 2001 Conference*, 2001.
12. Dahms, R., Fansler, T. D., Drake, M. C., Kuo, T.-W. et al., "Modeling Ignition Phenomena in Spray-Guided Spark-Ignited Engines," *Proceedings of the Combustion Institute* 32(2):2743-2750, 2009.
13. Lucchini, T., Cornolti, L., Montenegro, G., D'Errico, G. et al., "A Comprehensive Model to Predict the Initial Stage of Combustion in SI Engines," SAE Technical Paper 2013-01-1087, 2013, doi:10.4271/2013-01-1087.
14. Choi, C. R. and Huh, K. Y., "Development of a Coherent Flamelet Model for a Spark-Ignited Turbulent Premixed Flame in a Closed Vessel," *Combustion and Flame* 114:336-348, 1998.
15. Weller, H. G., Tabor, G., Gosman, A. D., and Fureby, C., "Application of a Flame Wrinkling LES Combustion Model to a Turbulent Mixing Layer," in *Proceedings the Twenty-Seventh Symposium on Combustion, The Combustion Institute*, 1998, 899-907.
16. Lucchini, T., D'Errico, G., Onorati, A., Bonandrini, G. et al., "Development of a CFD Approach to Model Fuel-Air Mixing in Gasoline Direct-Injection Engines," SAE Technical Paper 2012-01-0146, 2012, doi:10.4271/2012-01-0146.
17. Lucchini, T., D'Errico, G., Onorati, A., Bonandrini, G. et al., "Development and Application of a Computational Fluid Dynamics Methodology to Predict Fuel-Air Mixing and Sources of Soot Formation in Gasoline Direct Injection Engines," *International Journal of Engine Research* 15(5):581-596, 2014.
18. Gulder, O. L., "Turbulent Premixed Flame Propagation Models for Different Combustion Regimes," in *Proceedings the Twenty-Third Syposium on Combustion (International)*, 1990, 743-750.
19. Maly, R. R. and Herweg, R., "A Fundamental Model for Flame Kernel Formation in SI Engines," SAE Technical Paper 922243, 1992, doi:10.4271/922243.
20. Paredi, D., Lucchini, T., D'Errico, G., Onorati, A. et al., "Gas Exchange and Injection Modeling of an Advanced Natural Gas Engine for Heavy Duty Applications," SAE Technical Paper 2017-24-0026, 2017, doi:10.4271/2017-24-0026.
21. Lucchini, T., Della Torre, A., D'Errico, G., Onorati, A. et al., "A Comprehensive Methodology for Computational Fluid Dynamics Combustion Modeling of Industrial Diesel Engines," *International Journal of Engine Research* 18(1-2):26-38, 2017.
22. Lawes, M., Ormsby, M. P., Sheppard, C. G. W., and Woolley, R., "The Turbulent Burning Velocity of Iso-Octane/Air Mixtures," *Combustion and Flame* 159(5):1949-1959, 2012.
23. Lucchini, T., Della Torre, A., D'Errico, G., Montenegro, G. et al., "Automatic Mesh Generation for CFD Simulations of Direct-Injection Engines," SAE Technical Paper 2015-01-0376, 2015, doi:10.4271/ 2015-01-0376.
24. Lucchini, T., D'Errico, G., Jasak, H., and Tukovic, Z., "Automatic Mesh Motion with Topological Changes for Engine Simulation," SAE Technical Paper 2007-01-0170, 2007, doi:10.4271/2007-01-0170.
25. Montanaro, A., Allocca, L., Ettorre, D., Lucchini, T. et al., "Experimental Characterization of High-Pressure Impinging Sprays for CFD Modeling of GDI Engines," SAE Technical Paper 2011-01-0685, 2011, doi:10.4271/2011-01-0685.
26. Huh, K. Y. and Gosman, A. D., "A Phenomenological Model of Diesel Spray Atomization," in *Proceedings of the International Conference on Multiphase Flows*, Tsukuba, Japan, 1991.
27. Reitz, R. D., "Modeling Atomization Processes in High Pressure Vaporizing Sprays," *Atomization and Spray Technology* 3:309-337, 1987.
28. Huang, C., "Numerical Modelling of Fuel Injection and Stratified Turbulent Combustion in a Direct-Injection Spark-Ignition Engine Using an Open-Source Code," PhD thesis, Chalmers University of Technology, Sweden, 2014.
29. Amsden, A. A., O'Rourke, P., and Butler, T. D., "KIVA-II: A Computer Program for Chemically Reactive Flows with Sprays," LA-11560-MS, 1989.
30. Schetz, J. A. and Fuhs, A. E., *Handbook of Fluid Dynamic and Fluid Machinery*. Vol. 1 (Wiley Interscience).
31. Aleiferis, P. G. and Van Romunde, Z. R., "An Analysis of Spray Development with Iso-Octane, N-Pentane, Gasoline, Ethanol and N-Butanol from a Multi-Hole Injector under Hot Fuel Conditions," *Fuel* 105:143-168, 2013.
32. Zuo, B., Gomes, A. M., and Rutland, C. J., "Modeling Superheated Fuel Sprays and Vaporization," *Journal of Engine Research*, 2001.

33. Lucchini, T., D'Errico, G., and Nordin, N., "CFD Modeling of Gasoline Sprays," SAE Technical Paper 2005-24-086, 2005, doi:10.4271/2005-24-086.

34. Lucchini, T., D'Errico, G., Brusiani, F., Bianchi, G. M. et al., "Multi-Dimensional Modeling of the Air/Fuel Mixture Formation Process in a PFI Engine for Motorcycle Applications," SAE Technical Paper 2009-24-0015, 2009, doi:10.4271/2009-24-0015.

35. Weller, H. G., "The Development of a New Flame Area Combustion Model Using Conditional Averaging," Thermo-Fluids Section Report TF 9307, Imperial College of Science, Technology and Medicine, 1993.

36. Weller, H. G., Tabor, G., Gosman, A. D., and Fureby, C., "Application of a Flame-Wrinkling LES Combustion Model to a Turbulent Mixing Layer," in *Proceedings of the Twenty-Seventh Combustion Symposium (International)*, 1998.

37. Yang, X., Solomon, A., and Kuo, T., "Ignition and Combustion Simulations of Spray-Guided SIDI Engine Using Arrhenius Combustion with Spark-Energy Deposition Model," SAE Technical Paper 2012-01-0147, 2012, doi:10.4271/2012-01-0147.

38. Bray, K. N. C., *Studies of the Turbulent Burning Velocity* (1990), 315-335.

39. Lucchini, T., D'Errico, G., Onorati, A., Frassoldati, A. et al., "Modeling Non-Premixed Combustion Using Tabulated Kinetics and Different Flame Structure Assumptions," *SAE International Journal of Engines* 10(2):593-607, 2017, doi:10.4271/2017-01-0556.

40. Borghi, R., "On the Structure of Turbulent Premixed Flames," . In: Bruno C., Casci C., editors. *Recent Advances in Combustion Science*. (Pergamon, 1984).

41. Senda, J., Hojyo, Y., and Fujimoto, H., "Modelling of Atomization Process in Flash Boiling Spray," SAE Technical Paper 941925, 1994, doi:10.4271/941925.